International Journal of Thermofluids 20 (2023) 100412

Contents lists available at ScienceDirect

International Journal of Thermofluids

journal homepage: www.elsevier.com/locate/ijtf

Numerical investigation of an inertization system for a radiative coil coating oven

Bruno A.C. Barata [a,*], Jorge E.P. Navalho [a,b], José C.F. Pereira [a]

[a] IDMEC, Instituto Superior Técnico, Universidade de Lisboa, 1049-001 Lisboa, Portugal
[b] Departamento de Engenharia Mecânica e Industrial, Faculdade de Ciências e Tecnologia, Universidade Nova de Lisboa, 2829-516 Caparica, Portugal

ARTICLE INFO

Keywords:
Inertization chamber
Plane impinging jet
Moving flat plate
RANS
Numerical simulation

ABSTRACT

In this work the inertization of a radiative curing oven for coil coating is numerically investigated. Inertization chambers (IC) — comprised by a confined impinging slot jet and an exhaust slot — are applied at the curing oven openings to prevent external air from entering and toxic solvents from exiting the oven, avoiding simultaneously the contamination of the external surroundings and the development of explosive conditions within the oven. The influence of the main IC operating parameters — extracted-to-injected mass flow rate ratio (Ψ), coil plate-to-jet velocity ratio, injection Reynolds number, and oven pressure — on the safety of the sealing process is investigated considering the validated k-kl-ω transition RANS model. To guarantee safety conditions regarding the IC placed at the metal strip entrance, the corresponding range for Ψ was found to be between 0.8 and 1.6 considering oven pressures ranging from −20 to 20 Pa. For the IC placed at the metal strip exit and considering high coil velocities, safety conditions can only be observed with negative oven pressures. Overall, this procedure found a Ψ range between 0.8 and 1.2 that complies with the restrictive safety criteria for a realistic oven operation with typical coil velocities and oven pressures ranging from −20 to 10 Pa.

1. Introduction

The application of inertization processes is required in many production cycles that generate hazardous solids, liquids, and gases. The inert gas prevents the formation of explosive mixtures, being the oxygen volume fraction decreased to below the maximum allowable oxygen concentration (MAOC) to avoid the mixture from igniting — see *e.g.* Benazzoli [1]. Also, aerodynamic sealing by means of air curtains is used to separate/reduce the heat and mass exchange between two environments while allowing the passage of people and/or materials between these environments, as in the doorway of a ventilated building — see *e.g.* Frank and Linden [2], Ruiz et al. [3], and Viegas et al. [4]. There is a wide range of applications of these aerodynamic sealing and inertization techniques — see *e.g.* Hoppe and Jaeger [5] for chemical and fire safety, Xu et al. [6] for the mining industry, and Lin et al. [7] for moisture contamination control. For many applications involving industrial furnaces or ovens with openings, where the material is continuously fed through, aerodynamic sealing is required to avoid contamination of the surrounding atmosphere as well as air entrainment into the plant, which could lead to an explosive danger of highly flammable gases.

In the present study, the inertization of a radiative oven for coil coating is considered. In the coil coating process, a thin layer of solvent-based coating material is applied to metal substrates that are provided to a coil coating line in the form of a continuous thin and flat metal strip. This process increases the durability, corrosion resistance, and aesthetics of bare metal substrates, as well as provides enhanced optical properties for energy-saving concerns — see *e.g.* Sander [8], Rossi et al. [9,10], Gupta et al. [11], and Joudi et al. [12]. Radiative heat required to support coating drying and curing is supplied by radiant porous burners fed with highly flammable volatile organic compounds (VOCs) — solvent species collected in the oven after the evaporation from the applied wet coatings onto the metal strip took place. This technique is carried out continuously and closes the loop between the VOCs released and the fuel required to operate the burners. This is a novel curing oven operating solution that improves the system's compactness and energy efficiency and boosts production flexibility. Fig. 1 presents the three-dimensional (3D) geometry of the coil coating oven. The oven is comprised by a unit for IR radiative heat generation termed as the radiant burner section (RBS) and a unit where the coating drying and curing is carried out. The RBS is placed atop the COS module. The outlet section of porous radiant burners, which provides the IR radiant heat, is located at the RBS's ceiling, facing the COS, where a continuous metal strip is moving. The coated metal strip is heated by IR radiation, performing the drying and curing process in an atmosphere with solvent vapours, which are recirculated to increase efficiency. An IR-transparent glass window partition is installed between

* Corresponding author.
E-mail address: bruno.a.c.barata@tecnico.ulisboa.pt (B.A.C. Barata).

https://doi.org/10.1016/j.ijft.2023.100412
Received 15 May 2023; Received in revised form 29 June 2023; Accepted 29 June 2023
Available online 4 July 2023

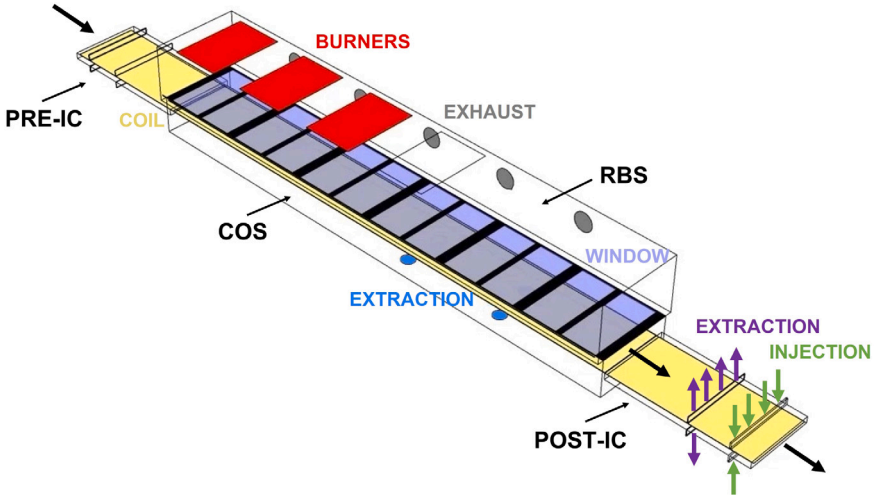

Fig. 1. Radiative coil coating oven.

the two modules to prevent the RBS and COS atmospheres from mixing while also allowing radiative heat transfer from the burners' surfaces to the paint film. The overall performance of this radiative coil coating furnace concept was investigated recently — see Barata et al. [13].

For a suitable oven operation, any leakage of the COS atmosphere as well as any external air entrainment into the COS should be prevented. For radiative curing ovens operating with radiant porous burners — as herein proposed —, the sealing safety requirements are accomplished by applying inertization chambers (IC) at the COS entrance and exit sections of the metal strip. (The oven sealing issue is not of major concern in conventional coil coating ovens relying on the convective air-drying technology since the injection of large amounts of heated air ensures negligible solvent losses to the surrounding environment and mixture conditions within the oven well below the lower explosive limit.) In the inertization chambers (pre–IC and post–IC), cooled flue gas is injected near the COS entrance/exit section as a slot impinging jet on the metal strip and extracted through slots near the surrounding environment — see Fig. 1. The injected and extracted flue gas acts as a gaseous curtain between the external environment and the COS region. One of the major features of this sealing process is this combination of a confined slot impinging jet with an extraction slot located close to the inertization chambers openings to the atmosphere. This novel solution increases the safety, flexibility, and efficiency of the sealing process since there are two mixing layers between the two environments, and the extracted flow can be recirculated or safely released with no need for after-treatment processes, while previous aerodynamic sealing solutions for industrial applications were only composed by impinging jets — see *e.g.* Oliveira et al. [14]. In fact, while a simple air curtain (composed by an impinging jet) could present an explosion risk by the turbulent mixing of species or by the impinging jet detachment, this novel configuration minimizes this risk with the extraction system.

Confined impinging jets are used in many engineering applications such as drying and cooling continuous sheets of materials, cooling turbine blades, electronic cooling, metal quenching, among others — see *e.g.* Polat [15], Onah et al. [16], Chowdhury et al. [17], Thesiya et al. [18], and Plant et al. [19]. In addition, impinging jets may serve as air curtains, as already mentioned, restricting the transfer of heat and mass between two zones. These sealing curtains have uses in the food industry, the containment of polluted zones and fire protection, building energy conservation, among others — see *e.g.* Foster et al. [20], Chen et al. [21], and Khayrullina et al. [22].

The very large number of experimental and computational works dedicated to studying the flow and heat transfer of the turbulent impinging jet showed that the impinging jet heat transfer is strongly affected by the jet nozzle-to-plate distance (H/B), being B the plane jet width — see Zuckerman and Lior [23]. Moreover, at high H/B ratios (typically $H/B > 5$), the jet becomes unsteady, presenting flapping oscillations that hinder accurate steady Reynolds-averaged Navier–Stokes (RANS) calculations and large eddy simulation (LES) becomes required to capture Kelvin–Helmholtz vortices interaction with the impinging wall for the slot jets — see Kubacki and Dick [24] and Barata et al. [25]. Since the present work is focused on inertization chambers comprising an impinging jet with a low H/B ratio (equal to 4.8), a prohibitive number of LES simulations in the optimization study can be avoided. Nevertheless, the employed RANS model is validated also with a detailed LES simulation to better understand the main jet characteristics.

Moreover, for low H/B ratios, Gardon and Akfirat [26], and Ashforth-Frost et al. [27] reported a secondary peak in the distribution of heat transfer coefficient, besides the expected maximum heat transfer at the stagnation point. In addition, the turbulence profiles showed that the region of the secondary peak is also the region with the highest turbulence levels, indicating that the transition to turbulence is complete. For high H/B ratios, this secondary peak is absent. Dutta and Dewan [28] showed that, for an H/B ratio equal to 4, the RANS turbulence models with adjustments for transitional flow outperform other models in terms of capturing the stagnation Nusselt number as well as the position and value of the secondary peak. Hofmann et al. [29] and Barata et al. [30] also found that using the transitional flow model results in improved predictions of the secondary peak.

The main objective of the present work is to investigate the range required for the operating parameters of inertization chambers — applied to a coil coating radiative curing oven — that assures a safe oven operation, *i.e.*, a suitable sealing of the curing oven by inertization chambers for several operating conditions. Large eddy simulation of flow and scalar fields is analysed and RANS simulations are validated. A battery of simulations — more than one hundred — allows the optimization of the flow field and extracted-to-injected mass flow rate ratio (Ψ) safety range for the nominal operating condition and for a range of metal strip velocities, injection Reynolds numbers, and different COS pressures. The optimization is conducted with the aim to verify, for each scenario, if the inertization system is able to prevent the VOCs from escaping into the atmosphere and the atmospheric oxygen from penetrating into the oven.

The paper is organized as follows: Section 2 presents the geometry, the governing equations, and the turbulence model used, as well as the numerical methods and boundary conditions. Additionally, a grid independence study is conducted and the performance validation of the k-kl-ω transition RANS turbulence model is assessed. In Section 3, flow fields for the nominal operating condition obtained with RANS

and LES are analysed. After, the Ψ safety range for the nominal operating condition is presented, and the effect of the metal strip velocity — velocity at which the metal strip is provided to the inertization chambers and curing oven —, injection Reynolds number, and COS pressure is presented and discussed. The main conclusions of the study are provided in Section 4.

2. Models

2.1. Physical model

To guarantee the safe operation of the radiative oven, both inertization chambers need to prevent the entrance of oxygen from the outside environment — avoiding the formation of an explosive atmosphere — and seal up the solvents evaporated in the COS — avoiding any leakage to the atmosphere. Fig. 2 shows schematically the two-dimensional (2D) geometry and the computation domain used for both the pre–IC and post–IC. In the absence of metal strip movement, the flow in both ICs is similar. Regarding the cases with metal strip motion, the metal strip moves along the positive x-direction and negative x-direction for the pre–IC and post–IC, respectively.

For the nominal operating condition, cold flue gas (at 359.44 K) is injected near the IC–COS interface at a Reynolds number ($Re_i = V_i B/\nu$) equal to 1.3×10^4 towards the metal strip. The metal strip is moving at a plate-to-jet velocity ratio ($R = |U_p/V_i|$) equal to 0.012, and extracted through slots near the surrounding environment, acting as a gaseous curtain between the external environment (at 298.15 K) and the COS region (at 562.98 K). For the nominal operating condition, the extracted-to-injected mass flow rate ratio ($\Psi = \dot{m}_e/\dot{m}_i$) is equal to 1.2. The gas composition at each section is presented in Table 1.

Table 1
Gas composition on a molar basis at each section.

Species	COS	Injection	Atmospheric air
O_2	0.035	0.036	0.210
CO_2	0.095	0.097	–
H_2O	0.133	0.135	–
N_2	0.718	0.732	0.790
Solvent	0.019	–	–

2.2. Mathematical and numerical models

2.2.1. RANS model

In the RANS calculations, the flow field is assumed to be two-dimensional and the fluid was defined as a gas mixture involving O_2, H_2O, CO_2, N_2, and a representative solvent species. The mass, momentum, and energy equations — for steady flow in a time average formulation (RANS) — are given by Eqs. (1), (2), and (3), respectively, and the transport equation for a scalar variable is given by Eq. (4), where ϕ represents the species mass fractions and Γ_{eff} the effective diffusion coefficient.

$$\frac{\partial}{\partial x_i}\left(\rho u_i\right) = 0 \tag{1}$$

$$\frac{\partial}{\partial x_j}\left(\rho u_i u_j\right) = -\frac{\partial p}{\partial x_i} + \frac{\partial}{\partial x_j}\left[\mu\left(\frac{\partial u_i}{\partial x_j} + \frac{\partial u_j}{\partial x_i} - \frac{2}{3}\delta_{ij}\frac{\partial u_l}{\partial x_l}\right)\right] + \frac{\partial}{\partial x_j}\left(-\rho\overline{u_i' u_j'}\right) \tag{2}$$

$$\rho c_p \frac{\partial}{\partial x_i}\left(u_i T\right) = \frac{\partial}{\partial x_i}\left(k\frac{\partial T}{\partial x_i} - \rho c_p \overline{u_i' T'}\right) \tag{3}$$

$$\frac{\partial}{\partial x_i}\left(\rho u_i \phi - \Gamma_{eff}\frac{\partial \phi}{\partial x_i}\right) = S_\phi \tag{4}$$

To close the RANS equations, the Boussinesq hypothesis was employed to relate the Reynolds stresses ($-\rho\overline{u_i' u_j'}$) to the mean velocity gradients whereas the isotropic eddy diffusivity formulation was considered for the turbulent heat flux ($-\rho\overline{u_i' T'}$).

Moreover, the k-kl-ω transition turbulence model proposed by Walters and Cokljat [31] was considered in the calculations. This model is a three-equation eddy-viscosity type, which includes transport equations for turbulent kinetic energy (k), laminar kinetic energy (kl), and the inverse turbulent time scale (ω). More details of this model and its implementation in FLUENT can be found elsewhere [32].

Model solution was carried out with FLUENT 16.2 solver. The convection and diffusion terms were discretized using a second-order scheme and the solution was considered to attain convergence when the normalized residual of each variable was lower than 10^{-6}.

2.2.2. LES model

In the LES calculations, the Navier–Stokes equations are filtered with a top-hat filter from the finite volume method used — see Eqs. (5) and (6).

$$\frac{\partial}{\partial x_i}\left(\rho\bar{u}_i\right) = 0 \tag{5}$$

$$\frac{\partial}{\partial t}\left(\rho\bar{u}_i\right) + \frac{\partial}{\partial x_j}\left(\rho\bar{u}_i\bar{u}_j\right) = -\frac{\partial\bar{p}}{\partial x_i} + \frac{\partial}{\partial x_j}\left[\mu\left(\frac{\partial\bar{u}_i}{\partial x_j} + \frac{\partial\bar{u}_j}{\partial x_i} - \frac{2}{3}\delta_{ij}\frac{\partial\bar{u}_l}{\partial x_l}\right)\right] - \frac{\partial\tau_{ij}}{\partial x_j} \tag{6}$$

From this filtering procedure results the sub-grid scale (SGS) stresses ($\tau_{ij} = \overline{\rho u_i u_j} - \rho\bar{u}_i\bar{u}_j$) that require modelling. The Boussinesq hypothesis was applied for the sub-grid scale turbulence models, and the turbulent viscosity at the sub-grid scale was modelled using the dynamic Smagorinsky–Lilly model [33,34]. In this model the Smagorinsky constant (required for computing the mixing length for sub-grid scale) is dynamically computed based on the information supplied by the resolved scales of motion.

LES calculations were also carried out using FLUENT 16.2 solver. The convective diffusive terms were discretized using a bounded central-difference scheme and a second-order central scheme, respectively. An implicit temporal discretization scheme was used and the maximum CFL in the domain was less than 1 to 5. The statistics were calculated for a sufficient number of jet revolutions that lead to a steady time-averaged velocity field. At each time step, the solutions were assumed to be converged when residuals of all the equations decreased three orders of magnitude.

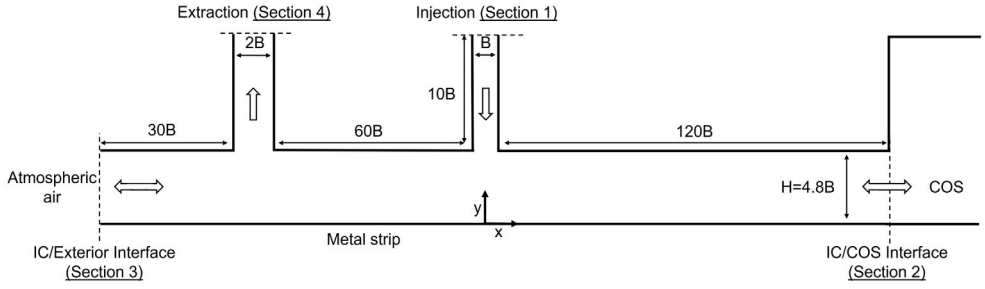

Fig. 2. 2D geometry of the inertization chamber.

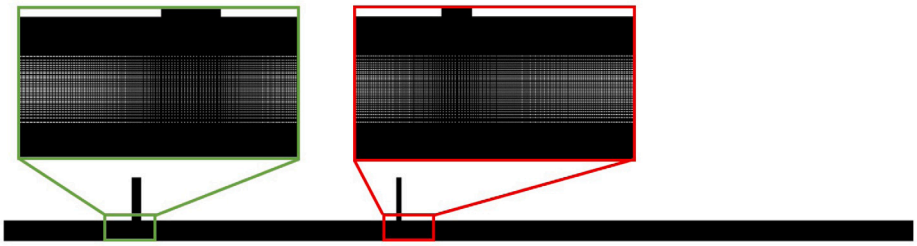

Fig. 3. Spatial discretization (mesh) of the computational domain with zoom in the inlet and outlet slots.

2.2.3. Boundary conditions

For both model techniques, at the injection, a uniform velocity profile (V_i) was specified based on the value of the Reynolds number ($Re = V_i B/\nu$, where B is the slot width). Additionally, a non-slip boundary condition was applied at the walls of the computational domain. The confinement surface was considered adiabatic. The metal strip moves at a velocity U_p, corresponding to a plate-to-jet velocity ratio (R) equal to $|U_p/V_i|$. Outlet boundary conditions were applied at both outlet sections, assuming atmospheric pressure. Moreover, the influence of the pressure inside the COS section (CP) is analysed. At the extraction section, a target mass flow rate was specified based on the value of the extracted-to-injected mass flow rate ratio ($\Psi = \dot{m}_e/\dot{m}_i$).

For LES calculations, the fluctuations were produced using the spectrum synthesizer method. Periodic boundary conditions were imposed in the z-direction since the transverse dimension $Z/B = \pi$ was considered large enough to capture the flow's greatest features according to Voke et al. [35].

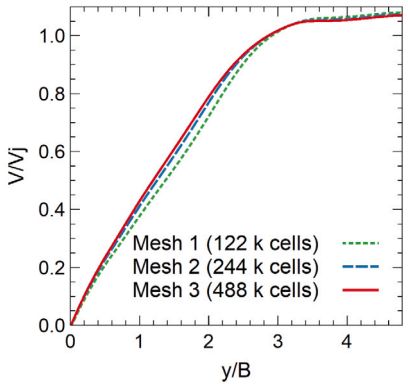

Fig. 4. Centreline y-velocity component profiles for the three meshes.

2.3. Grid independence study

A non-uniform mesh was considered for the RANS study with grid points concentrated near the impingement surface (assuring $y^+ \approx 1$) and around the injection and extraction centrelines (see Fig. 3) to capture the strong gradients and high shear zones in these zones.

Three meshes were selected to conduct a grid convergence study: Mesh 1 (122 k points); Mesh 2 (244 k points); and Mesh 3 (488 k points). For the nominal operating condition (considering a stationary plate), the pressure at the stagnation point calculated with the k-kl-ω transition model predicted 676.15, 677.99, and 678.98 Pa for the Meshes 1, 2, and 3, respectively. The order of convergence p was estimated and the grid convergence index (GCI) proposed by Roache [36] was computed for Mesh 2 and Mesh 3, considering a factor of safety of 1.25 since three grids were used to estimate p. The GCI for Mesh 2 and Mesh 3 is 0.0039 and 0.0021, respectively. Therefore, $\Lambda = 1$ and the solutions are in the asymptotic range of convergence. Moreover, Fig. 4 shows the vertical velocity along the centreline — which is often used to characterize the jet impinging on a stationary surface — using the k-kl-ω transition model and the three meshes, for the mentioned scenario. It is observed that beyond Mesh 2 no further significant change in the vertical velocity distribution is noticed. Therefore, Mesh 2 is able to describe the flow field virtually identically to a mesh with a higher cell density, and, consequently, this mesh is considered in all subsequent RANS calculations.

Furthermore, the mesh considered for the LES simulations was similar to the one used for the RANS simulations with non-uniform x and y grid spacings to correctly characterize the strong gradient zones. The mesh was expanded uniformly in the z-direction, presenting a total of 4 million points.

2.4. RANS turbulence model validation

The performance of the k-kl-ω transition RANS turbulence model to predict the flow field and heat transfer from a plane air impinging jet on a stationary plate with a low H/B ratio is addressed in this subsection. A simple computational domain was used. At the inflow, a uniform velocity profile was specified based on the value of the jet Reynolds number. Moreover, the turbulence intensity and the Reynolds number were specified in accordance with the data presented in each study. The jet inlet was set at ambient temperature. Additionally, a non-slip boundary condition was applied at the walls of the computational domain. The confinement surface was considered adiabatic. A higher temperature than the ambient one was imposed at the impingement plate. Outlet boundary conditions (at a distance equal to $100B$) were applied at both outlet sections, assuming atmospheric pressure.

Fig. 5(a) shows the distribution of the vertical velocity along the centreline obtained numerically with the k-kl-ω transition turbulence model. The result is presented for $H/B = 5$ and for $Re = 2.7 \times 10^4$, as considered in the experiments reported by Maurel and Solliec [37]. Fig. 5(b) shows the distribution for $Re = 2 \times 10^4$ and $H/B = 4$, in the range $0 < x/B < 12$, of the Nusselt number. The result of the k-kl-ω transition RANS turbulence model is compared with the experimental result from Ashforth-Frost et al. [27]. Finally, Fig. 5(c) shows the distribution, for $Re = 1.8 \times 10^4$ and $H/B = 4$, of the skin friction coefficient ($C_f = \tau_w/0.5\rho V_j^2$), in the range $0 < x/B < 12$. The result of the k-kl-ω transition RANS turbulence model is compared with the experiments of Dogruoz [38].

Fig. 5(a) shows a very good agreement of the profile of the vertical velocity using the k-kl-ω transition RANS turbulence model with the experimental data.

Fig. 5(b) shows that the predicted Nusselt number at the stagnation point by the k-kl-ω transition RANS turbulence model matches the experimental result. Moreover, the k-kl-ω transition model is able to correctly predict both the size and location of the Nusselt number secondary peak, presenting an off-stagnation minimum of about $0.5Nu_{st}$ at $x/B \approx 3$, and a secondary maximum of about $0.71Nu_{st}$ at $x/B \approx 8$, while the experimental work [27] predicted an off-stagnation minimum of $0.5Nu_{st}$ at $x/B \approx 3$ and a secondary maximum of $0.69Nu_{st}$ at $x/B \approx 7.4$.

Finally, Fig. 5(c) shows that the skin friction coefficient distribution has a minimum value of zero at the stagnation point indicating

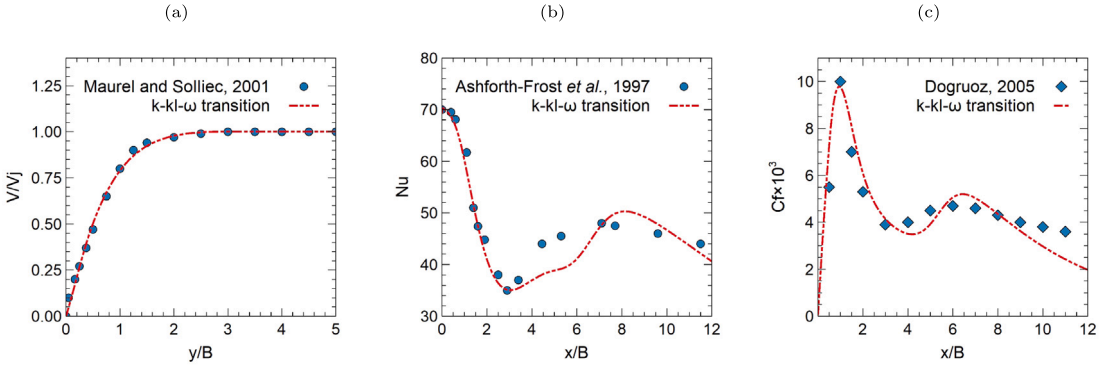

Fig. 5. RANS turbulence model validation for: (a) centreline y-velocity; (b) Nusselt number along $0 < x/B < 12$; and (c) skin friction coefficient distribution along $0 < x/B < 12$.

that there is no streamwise flow over the impingement surface. Just downstream of the stagnation point, it attains the peak value indicating a maximum streamwise velocity along and close to the impingement wall. Then, the secondary peak is observed followed by a monotonically decrease in the streamwise direction as the streamwise velocity near the impingement surface decreases. This trend is in line with the experimental work of Dogruoz [38].

3. Results and discussion

3.1. Nominal operating condition

In this subsection, the flow field and species concentration distribution will be analysed for the nominal operating condition ($\Psi = 1.2$, $Re_i = 1.3 \times 10^4$, $CP = 0$ Pa, and considering a stationary plate, *i.e.*, $R = 0$) through instantaneous and time-averaged LES data. Moreover, the performance of the k-kl-ω transition RANS turbulence model to predict the flow field and species concentration distribution for the same operating condition will be analysed, in order to assess the reliability of this model for the numerical optimization of the inertization process.

3.1.1. LES

Firstly, in order to inspect overall the flow field as well as the safety and sealing of the curing oven in the curing process, Fig. 6(a) shows the streamlines and the velocity magnitude plots for the considered scenario obtained by time-averaged LES. Moreover, Fig. 6(b), (c), and (d) present the mole fraction of O_2, CO_2, and solvent inside the IC, respectively, also obtained with time-averaged LES.

Overall, from Fig. 6(a) it is notable that the extraction channel creates a leftward shear force on the fluid resulting in a distorted flow field with the impinging jet deviating to the left. More concretely, the impinging jet preserves its verticality only along the beginning of the potential core due to its initial momentum. Then, the jet experiences deflection towards the exhaust slot, especially at the bottom level. Consequently, the impinging jet does not present the typical symmetrical flow field, with an impingement point with zero velocity at the jet centreline. Moreover, two recirculation zones can be observed in the off-stagnation regions, due to both jet entrainment and the presence of the confinement wall. The left recirculation region is clockwise, and the right recirculation region is counter-clockwise. Then, the flow reattaches to the confinement wall, reversing its direction. Additionally, it is possible to verify the entrainment of ambient air that is extracted, since for this operating condition $\Psi = 1.2$, meaning that the extracted mass flow rate is 1.2 times higher than the injected mass flow rate. From Fig. 6(b), it is notable that the IC is able to block the oxygen entrainment from the outside environment to reach the COS section. Fig. 6(c), shows that the injected flow (with 0.097 of CO_2 on a molar basis) does not reach the outside environment and, from Fig. 6(d), that the solvents evaporated in the COS do not leak to the atmosphere or the extraction channel. Therefore, the nominal operating condition is a safe operating scenario, since there is no risk of an explosive atmosphere within the COS, or leakage of solvent to the extraction system or the atmosphere.

Besides the analysis of the time-averaged LES flow field and species distribution, it is important to understand the temporal variations of the velocity field, in particular, the coherent structures resulting from the impinging jet. For that, Fig. 7 presents the instantaneous vortical structures by contours of the Q-criterion — which represents the balance between vorticity and strain rate, with a positive result meaning that the rotation overcomes the strain and shear, and vice-versa.

Overall, the vortical structures of the flow field are quite complex since they exist on both large and small scales and in a wide range of forms, showing how the vortices in the jet flow evolve and deform.

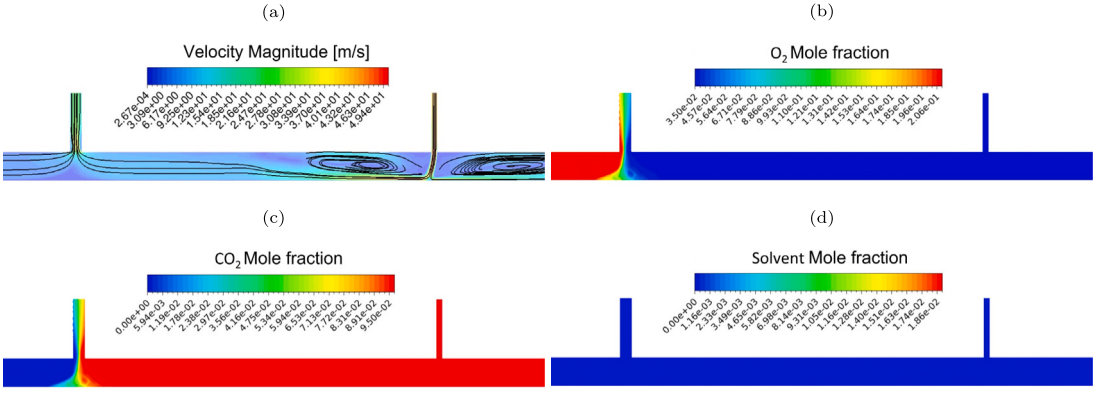

Fig. 6. Time-averaged LES results for the nominal operating condition and considering a stationary plate: (a) velocity magnitude and streamlines; (b) O_2 mole fraction; (c) CO_2 mole fraction; and (d) solvent mole fraction.

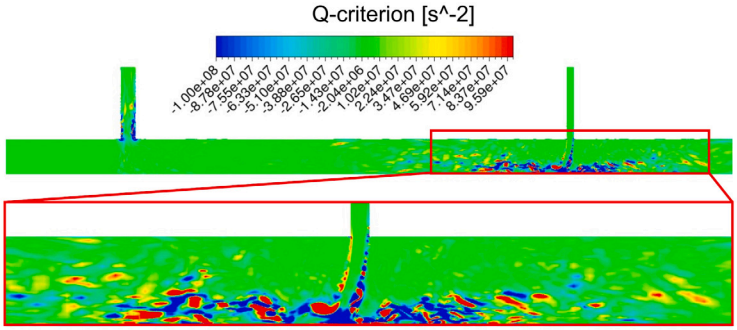

Fig. 7. Instantaneous contours of the Q-criterion in both the impinging jet and extraction channel.

Fig. 8. Instantaneous mole fraction inside the IC: (a) O_2; and (b) CO_2.

More concretely, it is notable that the initial vortices are induced in the two shear layers of the jet as a consequence of the Kelvin–Helmholtz instability. By merging with each other, larger structures are formed inducing the growth of the shear layer. Then, these structures experience a degree of stretching as they propagate downstream yielding bigger eddies in the intermediate region and smaller eddies as they get far away from the jet approaching the exhaust slot due to their breaking up.

The flow dynamics impacts the species transport inside the IC. Fig. 8(a) and (b) presents the instantaneous mole fraction distributions for O_2 and CO_2, respectively, in the IC.

Two major mechanisms are involved in mass transport between sections. The first is the advection due to the bulk movement of fluid driven by pressure gradients between the outlet, exhaust slot, and injection. The second is the eddies that approach the exhaust slot — as seen in Fig. 7 — which are responsible for some of the turbulent mixing. Fig. 8(a) and (b) clearly capture the dynamics of the mixing layer and the mechanisms of entrainment and mixing between flow from the jet and from the outlet.

3.1.2. RANS

In order to assess the performance of the k-kl-ω transition RANS turbulence model to predict the flow field and species concentration distribution, the time-averaged LES data is used for further comparison.

Fig. 9(a) shows the streamlines and the velocity magnitude plots for the considered scenario obtained by RANS. Moreover, Fig. 9(b), (c), and (d) present the mole fraction of O_2, CO_2, and solvent inside the IC, respectively, also obtained with RANS.

When comparing Fig. 9(a) with Fig. 6(a), it can be noticed that the flow close to the extraction channel is similar in both cases as well as the impingement point location — $x/B \approx -0.80$ for the RANS simulation and $x/B \approx -0.77$ for the time-averaged LES. The main difference between both solution fields is verified in the recirculation zones. Particularly, for the time-averaged LES, they are larger and farther from the jet axis, in comparison with the RANS simulation predictions.

Additionally, comparing Fig. 9(b), (c), and (d) against Fig. 6(b), (c), and (d), respectively, the safe operation of the process for the considered operating conditions can be verified in both approaches for solving the IC flow (RANS and LES). More concretely, the atmospheric oxygen does not reach the COS section (see Fig. 9(b)), the injected flow does not reach the outside environment (see Fig. 9(c)) and the solvent does not leak to the atmosphere or the extraction channel (see Fig. 9(d)).

In order to attain a deeper comparison between the species distribution, Fig. 10 presents the O_2 and CO_2 mole fraction profiles at $y/H = 0.5$ and $-5 \leq x/B \leq 5$, considering $x/B = 0$ as the extraction channel axis, for LES (time-averaged) and RANS approaches.

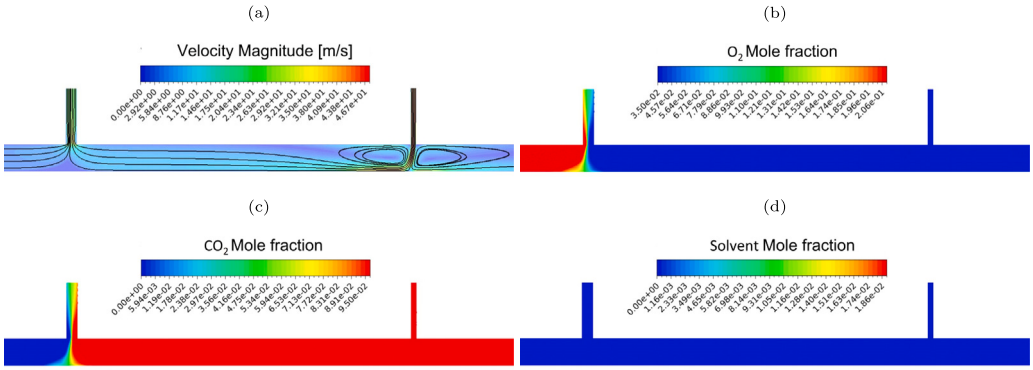

Fig. 9. RANS results for the nominal operating condition and considering a stationary plate: (a) velocity magnitude and streamlines; (b) O_2 mole fraction; (c) CO_2 mole fraction; and (d) solvent mole fraction.

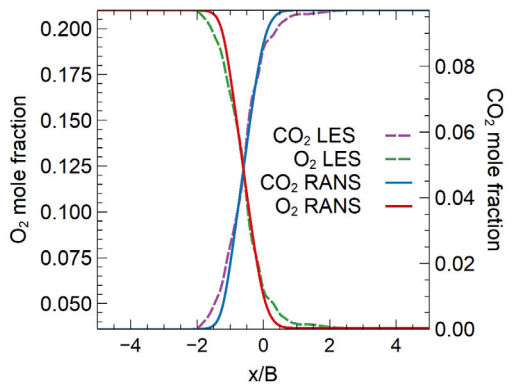

Fig. 10. O_2 and CO_2 mole fraction at $y/H = 0.5$ and $-5 \leq x/B \leq 5$ considering LES (time-averaged) and RANS approaches.

It can be observed an overall good agreement of the mixing layer using both approaches. Additionally, the time-averaged LES produces a slightly thicker mixing layer since this approach also considers the above-mentioned turbulence induced by the Kelvin–Helmholtz instabilities at the shear layer of the impinging jet that flows to the extraction channel.

Thus, the RANS approach is able to satisfactorily compute the time-averaged flow field close to the impinging jet and species diffusion close to the extraction channel, which is of paramount importance to accurately predict the performance of the chambers. Therefore, in the following optimization study the RANS approach can be applied, avoiding the need for a prohibitive number of LES simulations.

3.2. Optimization

An optimization of the inertization chambers operating parameters is herein conducted applying the RANS model. More concretely, the influencing parameters of the inertization process are the following:

(i) extracted-to-injected mass flow rate ratio (Ψ);
(ii) Reynolds number of the injected stream (Re_i);
(iii) COS pressure (CP); and
(iv) coil plate-to-jet velocity ratio (R).

The studied range of the mentioned operating parameters is listed in Table 2.

Table 2
Studied range of the inertization operating parameters.

Parameter	Minimum value	Maximum value
$\Psi = \dot{m}_e/\dot{m}_i$ [–]	0	2.8
$Re_i = V_i B/\nu$ [–]	7×10^3	1.9×10^4
CP [Pa]	−20	20
$R = \lvert U_p/V_i \rvert$ [–]	0	0.12

A particular operating condition (defined by a combination for the parameters listed in Table 2) is reliable (in full compliance with the safety requirements) if the following criteria were met:

(i) (Criterion C1) O_2 mole fraction at the IC/COS interface ($X^2_{O_2}$) lower than 0.036 (mole fraction of the injected flow), to avoid an explosive atmosphere;
(ii) (Criterion C2) CO_2 mole fraction at the IC/Exterior interface ($X^3_{CO_2}$) lower than 5000 ppm [39], to avoid contamination of surroundings;
(iii) (Criterion C3) solvent mole fraction at the extraction channel (X^4_{sol}) lower than 1 ppm [39], to avoid after-treatment processes; and
(iv) (Criterion C4) solvent mole fraction at the IC/Exterior interface (X^3_{sol}) lower than 1 ppm [39], to avoid contamination of surroundings.

This study is divided into three parts. Firstly, the influence of the extracted-to-injected mass flow rate ratio on the flow field and species distributions is analysed. Afterwards, the effect of the remaining operating parameter on the Ψ safety range is studied. Finally, considering the combined effect of the mentioned parameters, the full safety operating range is achieved.

3.2.1. Influence of the extracted-to-injected mass flow rate ratio

The influence of the extracted-to-injected mass flow rate ratio (Ψ) for $Re_i = 1.3 \times 10^4$, $R = 0$, and $CP = 0$ Pa is herein analysed. The Ψ ratio is an important parameter since it determines the suction created by the exhaust jet and, ultimately, the power required for the blowers. Thus, the Ψ ratio influences the direction of the flow at both ICs connections to the oven and to the atmosphere, which can result in the entrance of external air/COS atmosphere to the IC or the exit of the injected gas in both outlets.

Table 3 lists the mole fraction of the critical species at their critical sections. From Table 3, it can be verified that, for the considered operating scenario, the process is only safe when $0.8 \leq \Psi \leq 2.0$. Particularly, for Ψ equal to 0 and 0.4, some of the injected mass flow reaches the outlet section of the IC (infringing the Criterion C2), and, for Ψ equal to 2.4 and 2.8, the exhaust mass flow rate contains a non-negligible solvent mole fraction (violating the Criterion C3). More concretely, as Ψ increases from 2.4 to 2.8, the mole fraction of solvent at the extraction also increases. Moreover, for the studied range, the Criteria C1 and C4 are always respected, meaning that the atmospheric oxygen does not reach the COS section and the solvent does not reach the ICs outlet.

To improve the understanding of the causes of these two inertization failures, Fig. 11(a) and (b) compare the streamlines and the velocity magnitude plots for the mentioned scenarios considering $\Psi = 0.4$ and 2.8, respectively.

Comparing Fig. 11(a) with Fig. 9(a), it can be noticed that a smaller Ψ value affects the fluid flow. Particularly, for $\Psi = 0.4$, the impinging jet is less deviated — the impingement point is now at $x/B \approx -0.64$, with respect to the impinging jet centreline —, and no entrance of ambient air to the IC is verified since the extracted mass flow rate is smaller than the injected mass flow rate. In this case, the injected mass flow rate splits to the COS, the extraction system, and to the outlet (external environment). Comparing Fig. 11(b) with Fig. 9(a), it can be noticed that a higher Ψ value also significantly affects the fluid flow. In this case, the jet is totally deviated, presenting no impingement point and only the left recirculation region zone is present. In fact, contrary to what is typical in an impinging jet, the flow does not split into two wall jets. Instead, it only flows in the direction of the extraction channel, and thus entrance of the COS atmosphere to the IC is verified.

In order to verify the unsafe conditions for these two cases, Fig. 12(a), (c), and (e) present the mole fraction of O_2, CO_2, and solvent, respectively, in the IC for $\Psi = 0.4$ and Fig. 12(b), (d), and (f) present the same quantities but for $\Psi = 2.8$.

For $\Psi = 0.4$, Fig. 12(a) shows that no atmospheric oxygen enters the IC (it only contains the safe injection composition) however, from Fig. 12(c), it is noteworthy that the injected flow (with 0.097 of CO_2 in a molar basis) reaches the outside environment, being $\Psi = 0.4$ an unsafe operating condition. Moreover, Fig. 12(e) shows that the solvents evaporated in the COS do not enter the IC and, consequently, do not leak to the atmosphere or the extraction channel. For $\Psi = 2.8$, Fig. 12(b) shows that the IC is able to block the oxygen from the outside environment to reach the COS — note that the O_2 mole fraction decreases from the atmospheric value (0.21) to the injected value (0.036) across the extraction slot midplane section. From Fig. 12(d), it is notable that the injected flow does not reach the outside environment — the injected flow is totally extracted. Nevertheless, Fig. 12(f) shows that a non-negligible fraction of evaporated solvents in the COS is able to leak to the extraction channel, being $\Psi = 2.8$ an unsafe operating condition.

Table 3
Critical species mole fraction at different sections for different extracted-to-injected mass flow rate ratios. R (NR): Criterion Respected (Not Respected).

Ψ	$X^2_{O_2}$ (Criterion C1)	$X^3_{CO_2}$ (Criterion C2)	X^4_{sol} (Criterion C3)	X^3_{sol} (Criterion C4)
0	3.60×10^{-2} (R)	9.70×10^{-2} (NR)	0 (R)	0 (R)
0.4	3.60×10^{-2} (R)	9.70×10^{-2} (NR)	0 (R)	0 (R)
0.8	3.60×10^{-2} (R)	0 (R)	0 (R)	0 (R)
1.2	3.60×10^{-2} (R)	0 (R)	0 (R)	0 (R)
1.6	3.60×10^{-2} (R)	0 (R)	0 (R)	0 (R)
2.0	3.60×10^{-2} (R)	0 (R)	0 (R)	0 (R)
2.4	3.50×10^{-2} (R)	0 (R)	1.40×10^{-4} (NR)	0 (R)
2.8	3.50×10^{-2} (R)	0 (R)	1.14×10^{-3} (NR)	0 (R)

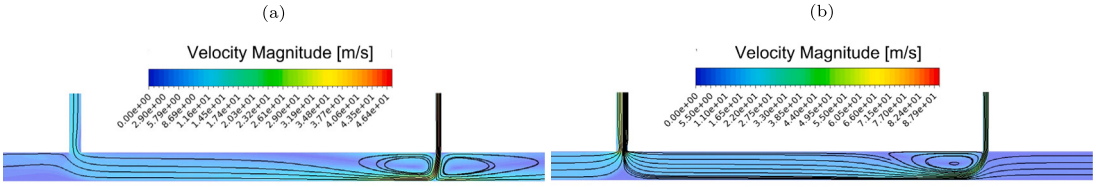

Fig. 11. Velocity magnitude and streamlines considering a stationary plate for $\Psi = 0.4$ (a) and $\Psi = 2.8$ (b).

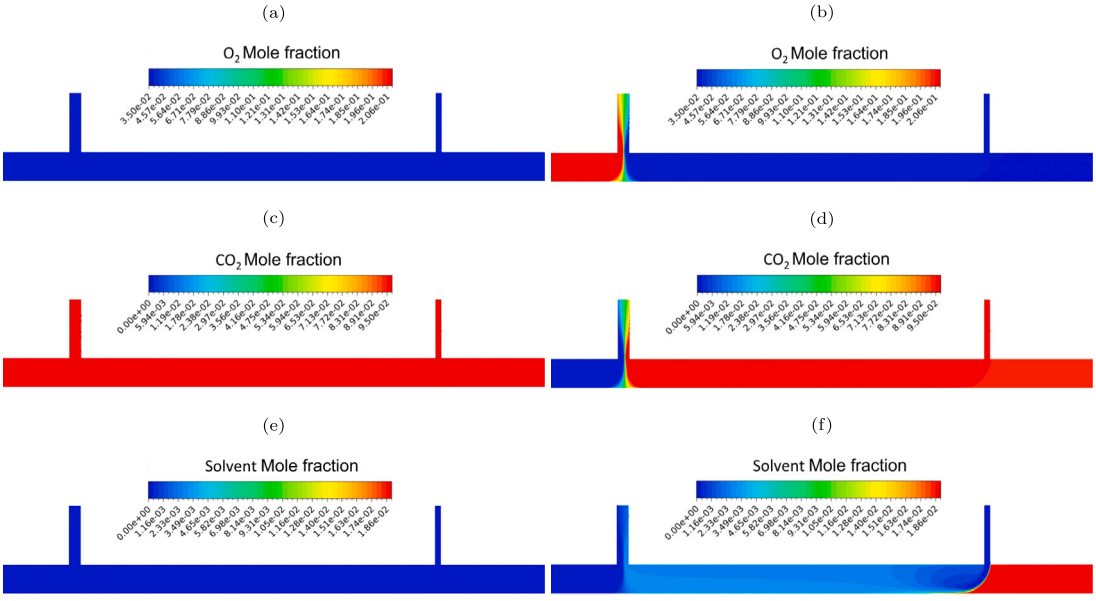

Fig. 12. Mole fraction inside the IC of: (a) O_2 ($\Psi = 0.4$); (b) O_2 ($\Psi = 2.8$); (c) CO_2 ($\Psi = 0.4$); (d) CO_2 ($\Psi = 2.8$); (e) solvent ($\Psi = 0.4$); and (f) solvent ($\Psi = 2.8$).

3.2.2. Parametric influence on the Ψ safety range

Besides the effect of the Ψ ratio, other parameters must be taken into consideration. Fig. 13(a)–(d) show the effect of the remaining inertization parameters on the Ψ safety range. More concretely, Fig. 13(a) shows the effect of the injection Reynolds number (for $R = 0$ and $CP = 0$ Pa), while Fig. 13(b) shows the effect of the COS pressure (for $R = 0$ and $Re_i = 1.3 \times 10^4$). Moreover, Fig. 13(c) and (d) show the effect of the R ratio (for $Re_i = 1.3 \times 10^4$ and $CP = 0$ Pa) at the pre–IC and post–IC, respectively. In Fig. 13(a)–(d), each point denotes a simulation and the circle symbol means that a safe operation is observed while the cross symbol indicates the violation of the safety rules.

Furthermore, Fig. 14(a), (b), and (c) show the mole fraction of solvent at the extraction channel (Criterion C3) dependence on Ψ and CP, Ψ and R at the pre–IC, and Ψ and R at the post–IC, respectively. In Fig. 14(a)–(c), each colour denotes a COS pressure/R ratio and the circle symbol means that the Criterion C3 is respected while the cross symbol indicates the violation of the Criterion C3.

Injection Reynolds number

Fig. 13(a) shows that the injection Reynolds number (Re_i), for the studied range, presents almost no effect on the IC operation. More concretely, the Ψ safety range is $0.8 \leq \Psi \leq 2.0$ for the five Reynolds numbers considered. Therefore, for the following cases, the considered injection Reynolds number is fixed at 1.3×10^4 since its effect on the Ψ safety range is negligible.

COS pressure

Since thermal processing in industrial ovens can take place in varied atmospheres, including pressures slightly above and below the standard atmospheric pressure, the effect of the COS pressure (CP) on the performance and safety of the process was also considered. For the negative COS pressures, the impinging jet is less deviated towards the extraction channel while for the positive COS pressures the impinging jet is more deviated (not shown). These modifications to the flow field also affect the safe operation of the IC. Fig. 13(b) shows that for both CP equal to −20 and −10 Pa, the Ψ safety range is $0.8 \leq \Psi \leq 2.4$. In fact, when the oven is operating at pressures below the standard

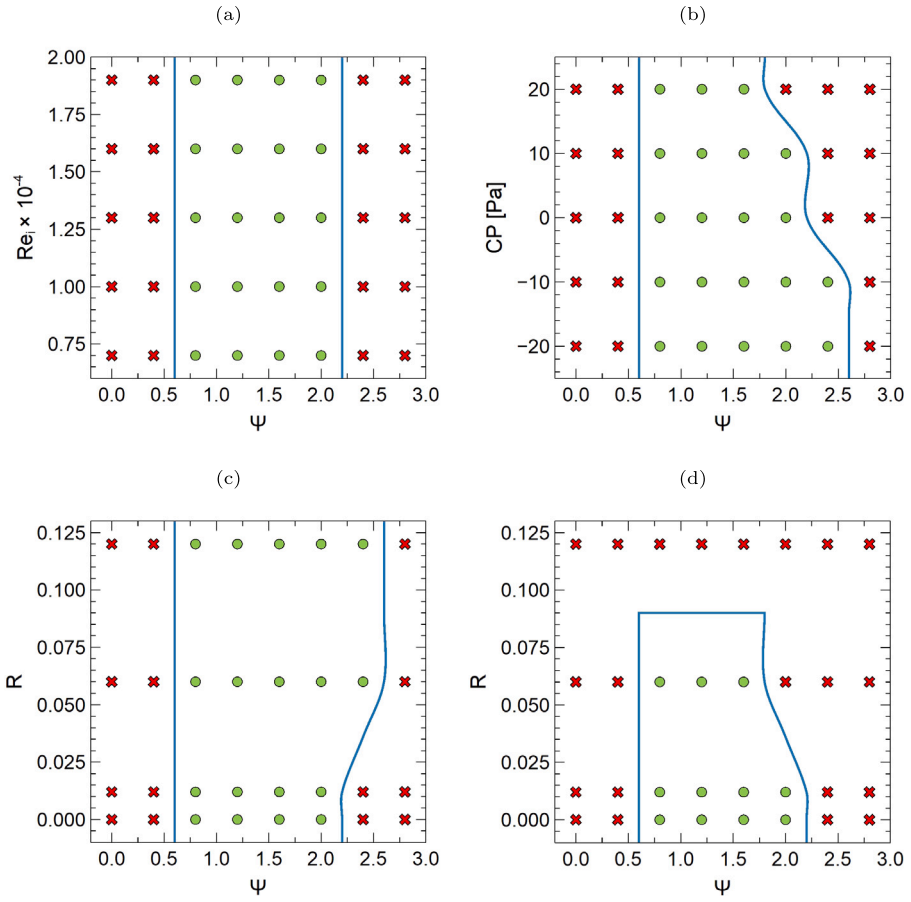

Fig. 13. Ψ safety range for the considered: (a) injection Reynolds number (Re_i) for $R = 0$ and $CP = 0$ Pa; (b) COS pressures (CP) for $R = 0$ and $Re_i = 1.3 \times 10^4$; (c) coil-to-jet velocity ratios (R) at the pre–IC for $Re_i = 1.3 \times 10^4$ and $CP = 0$ Pa; and (d) coil-to-jet velocity ratios (R) at the post–IC for $Re_i = 1.3 \times 10^4$ and $CP = 0$ Pa. Green dots (red crosses): safe (unsafe) operation.

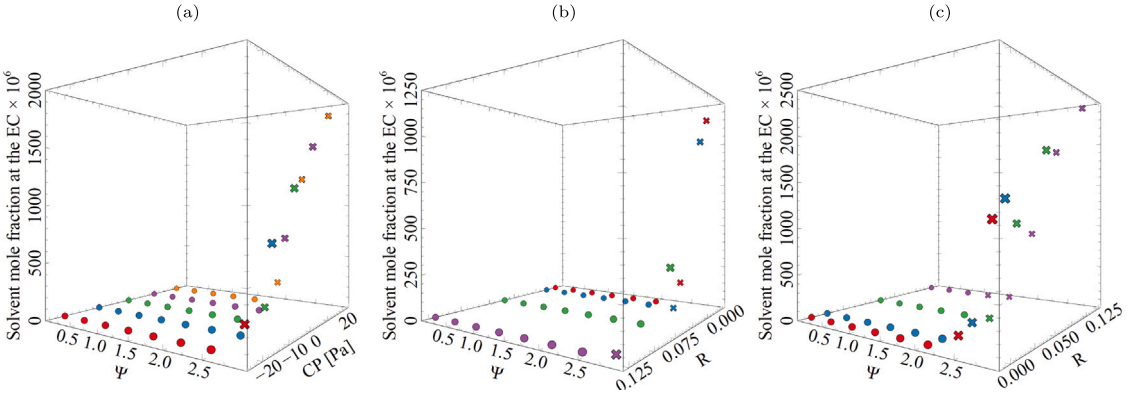

Fig. 14. Solvent mole fraction at the extraction channel (EC) for different extraction-to-injection mass flow rate (Ψ) values and different: (a) COS pressures (CP) for $R = 0$ and $Re_i = 1.3 \times 10^4$; (b) coil-to-jet velocity ratios (R) at the pre–IC for $Re_i = 1.3 \times 10^4$ and $CP = 0$ Pa; and (c) coil-to-jet velocity ratios (R) at the post–IC for $Re_i = 1.3 \times 10^4$ and $CP = 0$ Pa. Dots (crosses): Criterion C3 respected (violated).

atmospheric pressure, the jet is less deviated and the total deviation of the impinging jet and consequent leakage of solvent to the extraction channel (Criterion C3) occurs for a higher Ψ ratio. On the other side, for CP equal to 10 and 20 Pa, the operation is only safe for $0.8 \leq \Psi \leq 2.0$ and $0.8 \leq \Psi \leq 1.6$, respectively. When the oven is operating at pressures above the standard atmospheric pressure, the jet is more deviated and the total deviation of the impinging jet and consequent leakage of solvent the extraction channel occurs for a smaller Ψ ratio, as shown in Fig. 13(b). Consequently, the failures for the higher Ψ ratios are related to the total deviation of the impinging jet and thus the upper limit of the Ψ operation range is affected by the COS pressure. The failure for the smaller Ψ ratios ($\Psi = 0$ and 0.4) is still related to the injected flow reaching the outside environment (Criterion C2), and the COS pressure does not affect the lower limit of the Ψ operation range. Moreover, for all the cases the exterior air is not able to reach the oven (Criterion C1), and no solvent leaks to the outside of the IC (Criterion C4).

Additionally, from Fig. 14(a), for the same Ψ ratio, an increasing suction in the oven (negative pressure) decreases the mole fraction of solvent at the extraction channel while a more positive pressure

increases the mole fraction of solvent at the extraction channel. The most critical case occurs for $\Psi = 2.8$ and $CP = 20$ Pa.

Coil plate-to-jet velocity ratio

For the previous cases, a stationary impinging plate was considered ($R = 0$), however, the metal strip moves in the coil coating process. This movement originates high shear zones that have an impact on the flow field, especially on the two wall jets at the impingement plate since one of them flows in the plate movement direction and the other in the opposite direction. In fact, at the pre–IC the coil velocity deviates less the impinging jet, and, for high velocities, the jet can even deviate to the right. On the other side, at the post–IC, the coil velocity deviates more the impinging jet, and, for high velocities, a detachment point appears at the right wall jet that induces the development of a third recirculation zone (with a rotation opposite to that of the recirculation zone close to it — not shown). Consequently, the effect of the metal strip (coil) velocity on the impinging jet behaviour is more pronounced at the post–IC because the coil is moving from the injection to the extraction channel.

Thus, due to the highly changed flow field, the coil velocity affects the safety of the process. Fig. 13(c) shows that for the pre–IC the operation is still only safe when $0.8 \leq \Psi \leq 2.0$ for R equal to 0.012 while is safe when $0.8 \leq \Psi \leq 2.4$ for R equal to 0.06 and 0.12. Therefore, the increased plate velocity is able to increase the upper limit of the Ψ safety range for R equal to 0.06 and 0.12 since, similarly to the previous cases, the jet is less deviated and the total deviation of the impinging jet and consequent leakage of solvent to the extraction channel (Criterion C3) occurs for a higher Ψ ratio. The positive plate velocity still does not affect the lower limit of the Ψ operation range with the failure still being related to the injected flow reaching the outside environment (Criterion C2). Moreover, for all the studied cases no entrance of the exterior air into the oven (Criterion C1) and no solvent leakage to the outside (Criterion C4) is verified in the pre–IC.

Fig. 13(d) shows that for the post–IC the safe range is $0.8 \leq \Psi \leq 2.0$ and $0.8 \leq \Psi \leq 1.6$ for R equal to 0.012 and 0.06, respectively. Moreover, for R equal to 0.12 and for the studied Ψ range the operation is never safe. In fact, since the metal strip movement direction is towards the outlet, entrainment of the COS atmosphere is of extreme relevance for the higher velocity case. For $\Psi \geq 1.2$, the failure is caused by the entrainment of solvents into the extraction system (Criterion C3), while for $\Psi \leq 0.8$ flue gas is released to the surrounding environment through the post–IC outlet section (Criterion C2). Moreover, in some cases, the solvent is able to reach the post–IC outlet section but with an harmless concentration in such a way that Criterion C4 is still respected. Once more, for all the studied cases no entrainment of the exterior air into the oven is observed (Criterion C1).

Additionally, it is important to remark that for both the pre–IC and post–IC, the ratio R equal to 0.012 (typical in the coil coating process) produces no effect on the Ψ safety range, only changing slightly the mole fraction of solvent at the extraction channel for the Ψ ratios that lead to failure (Criterion C3).

Moreover, from Fig. 14(b), it can be noticed that, for the same Ψ ratio, a higher velocity at the pre–IC decreases the mole fraction of solvent at the extraction channel since the metal strip movement direction is towards the COS, increasing the difficulty of solvent leakage. On the other side, from Fig. 14(c), a higher velocity at the post–IC increases the mole fraction of solvent at the extraction channel since the metal strip movement direction is towards the outlet, allowing entrainment of the oven atmosphere and consequently decreasing the difficulty of solvent leakage. Moreover, comparing Fig. 14(b) and (c), for equal R and Ψ ratios, the safety of the process is more challenging at the post–IC.

3.2.3. Combined operation range

After the parametric study of several operating parameters, it is important to investigate their combined effect. In particular, the influence of the metal strip velocity and COS pressure on the Ψ safety range is analysed. The considered Reynolds number ($Re_i = 1.3 \times 10^4$) is fixed since, as concluded previously, its effect on the Ψ safety range is diminutive when compared with the other parameters.

Fig. 15 shows how the Ψ safety range is affected by the combined effect of the COS pressure and the R ratio (in both the pre–IC and post–IC). It can be verified that, for the same COS pressure, an increase of the plate velocity induces an increase of the Ψ safety range at the pre–IC and a decrease in the post–IC. Also, for the same plate velocity, a decrease of the COS pressure is able to increase the Ψ safety range. Moreover, for the case of $R = 0.12$ at the post–IC that was verified to operate unsafely for all the Ψ ratios ($CP = 0$ Pa), when considering negative COS pressures safety can be achieved. As expected, the most critical scenario of operation is at the post–IC when working with positive COS pressures and high coil velocities since a relevant amount of solvent is traced at the extraction channel and flue gas leakage from the IC to the surrounding environment can be observed. Thus, for the studied oven conditions (with a homogeneous oven atmosphere — pressure and mixture composition) and IC geometry operating with the same Ψ ratio and injection Reynolds number in both ICs, the safety of the process is governed by the post–IC performance since it is the most likely to fail for high metal strip velocities due to solvent entrainment to the extraction system. Moreover, Ψ ratios between 0.8 and 1.2 are able to provide compliance with all the stipulated safety criteria for a larger range of injection Reynolds numbers, oven pressures, and typical metal strip velocities.

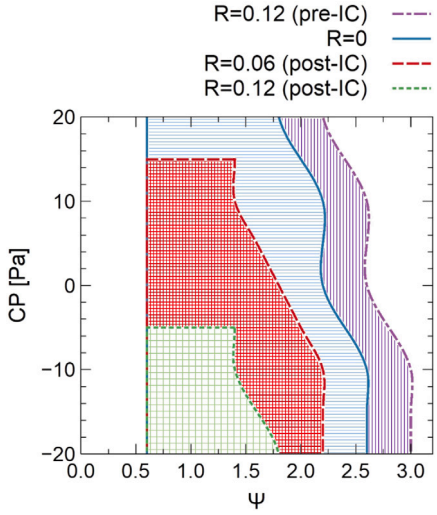

Fig. 15. Ψ safety range for the combined effect of the COS pressure and R ratio at the pre– and post–ICs.

4. Conclusions

In this work, an inertization system for a curing oven was considered with the objective to investigate numerically the safety and sealing for several operating conditions. The simple geometry of a confined slot impinging jet — one of the major features of this sealing process — was considered for the validation of the RANS k-kl-ω transition model. Additionally, the selected RANS model was also verified to be in satisfactory agreement with the time-averaged LES data for the inertization chamber (IC) operating at the nominal condition (for which $\Psi = 1.2$) and considering a stationary plate for simplicity.

For the previous operating condition, the main failure mechanisms were addressed by varying the extracted-to-injected mass flow rate ratio (Ψ). A safe operation was only found for Ψ along the range 0.8 to 2.0, since, for a small Ψ ratio, some of the injected mass flow rate

leaks to the outlet whereas, for a high Ψ ratio, a non-negligible fraction of VOCs is able to leak to the extraction channel. Furthermore, the parametric study allowed the conclusions that, for oven operating pressures below (above) the atmospheric pressure, the upper limit of the Ψ safety range increases (decreases). Additionally, when considering a non-negligible coil velocity, a higher velocity at the pre–IC (post–IC) increases (decreases) the upper limit of the Ψ safety range. Finally, an investigation combining the most relevant IC operating parameters revealed that the most critical operation scenario is observed at the post–IC for positive COS pressures and high coil velocities. Overall, this procedure found a Ψ range between 0.8 and 1.2 that complies with the restrictive safety criteria for a realistic oven operation with typical coil velocities and oven pressures ranging from −20 to 10 Pa.

Declaration of competing interest

The authors declare that they have no known competing financial interests or personal relationships that could have appeared to influence the work reported in this paper.

Data availability

Data will be made available on request.

Acknowledgements

This research was funded by the European Community's Framework Programme for Research and Innovation Horizon 2020 under grant agreement no. 768692 (ECCO). This work was also supported by Fundação para a Ciência e a Tecnologia, Portugal, through IDMEC, under LAETA, project UIDB/50022/2020.

References

[1] A. Benazzoli, Inertization's Project of Reactors Processing Volatile Organic Liquids (Master's Thesis), University of Padova, 2015.
[2] D. Frank, P. Linden, The effectiveness of an air curtain in the doorway of a ventilated building, J. Fluid Mech. 756 (2014) 130–164, http://dx.doi.org/10.1017/jfm.2014.433.
[3] C. Alanis Ruiz, T. Hooff, B. Blocken, G. Heijst, Air curtain performance: Introducing the adapted separation efficiency, Build. Environ. 188 (2021) 107468, http://dx.doi.org/10.1016/j.buildenv.2020.107468.
[4] J. Viegas, F. Oliveira, D. Aelenei, Experimental study on the aerodynamic sealing of air curtains, Fluids 3 (2018) 49, http://dx.doi.org/10.3390/fluids3030049.
[5] T. Hoppe, N. Jaeger, Reliable and effective inerting methods to prevent explosions, Process Saf. Prog. 24 (2005) 266–272, http://dx.doi.org/10.1002/prs.10098.
[6] G. Xu, K. Luxbacher, S. Ragab, x. Jialin, X. Ding, Computational fluid dynamics applied to mining engineering: a review, Int. J. Min. Reclam. Environ. 31 (2016) 1–25, http://dx.doi.org/10.1080/17480930.2016.1138570.
[7] T. Lin, O. Zargar, T.-C. Lee, D.L. Sabusap, J.-J. Li, S.-C. Hu, J. Khodadadi, D. Jamshideasli, G. Leggett, Flow analysis of a front opening unified pod (FOUP) subjected to different fan filter unit (FFU) coverage area in mini-environment, Int. J. Thermofluids 12 (2021) 100124, http://dx.doi.org/10.1016/j.ijft.2021.100124.
[8] J. Sander, Coil coating, 2019, http://dx.doi.org/10.1515/9783748602231.
[9] S. Rossi, F. Deflorian, J. Fiorenza, Environmental influences on the abrasion resistance of a coil coating system, Surf. Coat. Technol. 201 (2007) 7416–7424, http://dx.doi.org/10.1016/j.surfcoat.2007.02.008.
[10] S. Rossi, M. Calovi, D. Dalpiaz, M. Fedel, The influence of NIR pigments on coil coatings' thermal behaviors, Coatings 10 (2020) 514, http://dx.doi.org/10.3390/coatings10060514.
[11] G. Gupta, S. Pathak, A. Khanna, Anticorrosion performance of eco-friendly silane primer for coil coating applications, Prog. Org. Coat. 74 (2012) 106–114, http://dx.doi.org/10.1016/j.porgcoat.2011.11.023.
[12] A. Joudi, H. Svedung, M. Cehlin, Reflective coatings for interior and exterior of buildings and improving thermal performance, Appl. Energy 103 (2013) 562–570, http://dx.doi.org/10.1016/j.apenergy.2012.10.019.
[13] B.A.C. Barata, B.S. Dias, J.E.P. Navalho, M. Schneider, P. Weinbrecht, C. Weis, D. Trimis, J.C.F. Pereira, Numerical investigation of an innovative furnace concept for industrial coil coating lines, Therm. Sci. Eng. Prog. (2023) 101843, http://dx.doi.org/10.1016/j.tsep.2023.101843.
[14] L. Oliveira, J. Costa, M. Carvalho, H. Gerhardt, C. Kramer, On aerodynamic sealing for industrial applications, J. Wind Eng. Ind. Aerodyn. 37 (1991) 255–268, http://dx.doi.org/10.1016/0167-6105(91)90011-K.
[15] S. Polat, Heat and mass transfer in impingement drying, Drying Technol. 11 (1993) 1147–1176, http://dx.doi.org/10.1080/07373939308916894.
[16] E.D.T. Onah, B. Ekwueme, A. Odukwe, N. Nduka, A. Orga, E. Marcel, S. Chukwujindu, C. Diyoke, A. Nwankwo, C. Asogwa, A. Chikezie, K. Enebe, C. Asadu, Improved design and comparative evaluation of controlled water jet impingement cooling system for hot-rolled steel plates, Int. J. Thermofluids 15 (2022) 100172, http://dx.doi.org/10.1016/j.ijft.2022.100172.
[17] T. Shawkat Chowdhury, F. Mohsin, M. Tonni, M. Mita, M. Ehsan, A critical review on gas turbine cooling performance and failure analysis of turbine blades, Int. J. Thermofluids 18 (2023) 100329, http://dx.doi.org/10.1016/j.ijft.2023.100329.
[18] D. Thesiya, H. Patel, G. Patange, A comprehensive review electronic cooling: A nanomaterial perspective, Int. J. Thermofluids 19 (2023) 100382, http://dx.doi.org/10.1016/j.ijft.2023.100382.
[19] R. Plant, J. Friedman, Z. Saghir, A review of jet impingement cooling, Int. J. Thermofluids 17 (2023) 100312, http://dx.doi.org/10.1016/j.ijft.2023.100312.
[20] A. Foster, M. Swain, R. Barrett, P. D'Agaro, L. Ketteringham, S. James, Three-dimensional effects of an air curtain used to restrict cold room infiltration, Appl. Math. Model. 31 (2007) 1109–1123, http://dx.doi.org/10.1016/j.apm.2006.04.005.
[21] Z. Chen, Z. Liu, X. Li, H. Linqi, G. Niu, Numerical study of the effect of air curtains on smoke blocking and leakage heat flux in tunnel fires, Case Stud. Therm. Eng. 35 (2022) 102164, http://dx.doi.org/10.1016/j.csite.2022.102164.
[22] A. Khayrullina, T. Hooff, B. Blocken, G. van Heijst, PIV measurements of isothermal plane turbulent impinging jets at moderate Reynolds numbers, Exp. Fluids 58 (2017) http://dx.doi.org/10.1007/s00348-017-2315-0.
[23] N. Zuckerman, N. Lior, Jet Impingement Heat Transfer: Physics, Correlations, and Numerical Modeling, in: Advances in Heat Transfer, vol. 39, Elsevier, 2006, pp. 565–631, http://dx.doi.org/10.1016/S0065-2717(06)39006-5.
[24] S. Kubacki, E. Dick, Simulation of plane impinging jets with k-ω based hybrid RANS/LES models, Int. J. Heat Fluid Flow 31 (2010) 862–878, http://dx.doi.org/10.1016/j.ijheatfluidflow.2010.04.011.
[25] B.A.C. Barata, J.E.P. Navalho, J.C.F. Pereira, Prediction of self-sustained oscillations of an isothermal impinging slot jet, Fluids 8 (1) (2023) http://dx.doi.org/10.3390/fluids8010015.
[26] R. Gardon, J. Akfirat, Heat transfer characteristics of impinging two-dimensional air jets, J. Heat Transfer 88 (1966) 101, http://dx.doi.org/10.1115/1.3691449.
[27] S. Ashforth-Frost, K. Jambunathan, C. Whitney, Velocity and turbulence characteristics of a semiconfined orthogonally impinging slot jet, Exp. Therm Fluid Sci. 14 (1997) 60–67, http://dx.doi.org/10.1016/S0894-1777(96)00112-4.
[28] R. Dutta, A. Dewan, Comparison of various integration to wall (ITW) RANS models for predicting turbulent slot jet impingement heat transfer, Int. J. Heat Mass Transfer 65 (2013) 750–764, http://dx.doi.org/10.1016/j.ijheatmasstransfer.2013.06.056.
[29] H. Hofmann, R. Kaiser, M. Kind, H. Martin, Calculations of steady and pulsating impinging jets - an assessment of 13 widely used turbulence models, Numer. Heat Transfer B 51 (2007) 565–583, http://dx.doi.org/10.1080/10407790701227328.
[30] B.A.C. Barata, J.E.P. Navalho, J.C.F. Pereira, RANS simulations of plane impinging jets: On the influence of plate velocity in the nusselt number secondary peak, Therm. Sci. (2023) 127, http://dx.doi.org/10.2298/TSCI230206127B.
[31] D. Walters, D. Cokljat, A three-equation eddy-viscosity model for Reynolds-averaged Navier–Stokes simulations of transitional flow, J. Fluids Eng. Trans. ASME 130 (2008) http://dx.doi.org/10.1115/1.2979230.
[32] Ansys, Ansys Fluent Theory Guide, ANSYS, Inc, 2021.
[33] J. Smagorinsky, General circulation experiments with primitive equations, J. Fluid Mech. 104 (1963) 99–165.
[34] D. Lilly, A proposed modification of the germano subgrid-scale closure, Phys. Fluids A 4 (1994) 633–635.
[35] P. Voke, S. Gao, D. Leslie, Large-eddy simulations of plane impinging jets, Internat. J. Numer. Methods Engrg. 38 (1995) 489–507, http://dx.doi.org/10.1002/nme.1620380309.
[36] P. Roache, Perspective: A method for uniform reporting of grid refinement studies, J. Fluids Eng. Trans. ASME 116 (1994) 405–413, http://dx.doi.org/10.1115/1.2910291.
[37] S. Maurel, C. Solliec, A turbulent plane jet impinging nearby and far from a flat plate, Exp. Fluids 31 (2001) 687–696, http://dx.doi.org/10.1007/s003480100327.
[38] M. Dogruoz, Experimental and Numerical Investigation of Turbulent Heat Transfer due to Rectangular Impinging Jets (Ph.D. Thesis), University of Arizona, 2005.
[39] Occupational safety and health administration, 2022, Accessed: 2022-09-05. https://www.osha.gov/annotated-pels.